CHAPTER 2

ELECTROMAGNETIC ANALYSIS OF AN AXIALLY PERIODIC DISK-LOADED SLOW-WAVE STRUCTURE WITH LOW-LOSS DIELECTRIC FILLING BETWEEN DISKS FOR A MAGNETICALLY INSULATED LINE OSCILLATOR *

*Part of this work has been published as:

Nisheeth Upadhyay, Arjun Kumar, Prabhakar Tripathi and Smrity Dwivedi "Electromagnetic Analysis of an Axially Periodic Disk-Loaded Slow-Wave Structure With Low-Loss Dielectric Filling Between Disks for a Magnetically Insulated Line Oscillator," *IEEE trans. Plasma Sci.*, vol. 50, no. 4, pp. 825-834, Apr. 202

2.1 Outline

In this Chapter, the partially dielectrically filled periodic disk-loaded co-axial structure as a slow wave interaction structure for magnetically insulated transmission line oscillator (MILO) has been electromagnetically analyzed using field matching technique. A periodic disk-loaded coaxial structure in which the low-loss dielectric material is partially filled between subsequent discs is included in the slow wave structure (SWS).The dispersion relationship and interaction impedance were evaluated in the study, taking into consideration all of the harmonics generated inside the structure. The influence of the material's dielectric constant on dispersion characteristics and phase velocity has been studied. The influence of various structural factors on dispersion characteristics and interaction impedance has also been determined. The analytically derived dispersion results were compared with previously known dispersion results and then validated using the commercial code "Computer Simulation Tool (CST) Studio Suite" to validate the completed theoretical study. In terms of dispersion characteristics, the agreement between theoretical analysis and simulation is within 5%.

2.2 Introduction

In high-power microwave (HPM) sources, MILO has been extensively studied due to its attractive features such as compact size and ability to generate high-peak radio frequency (RF) power in several gigawatt ranges without any need of any external dc magnetic field [Benford *et al*., 2007-Clark *et al*., 1988-Lemke *et al., 1997*].The device is based on the relativistic discharge of electrons in a magnetically insulated region on which a slow wave structure (SWS) is imposed. The geometrical structure of MILO is analogous to linear magnetron [Lemke *et al.*, 1997]. For operation, MILO requires a very high input dc pulse voltage which is applied between the anode and cathode section. As a result,

explosive emissions take place and high-intensity relativistic electrons are emitted from the surface of the cathode. The high relativistic electrons that are emitted from the cathode move radially toward the anode and generate anode current which is also known as load current. When this load current exceeds the critical current, magnetic insulation is generated inside the device. This self-magnetic insulation property of the MILO guides the electron beam without requiring any external dc magnetic field which enables it to operate at very high voltages without any vacuum breakdown [Lemke *et al.*, *1998*]. Despite the various attractive features of MILO, the device suffers from the problem of low efficiency and pulse shorting [Lemke *et al.*, 1997]. Therefore, improving its conversion efficiency and overcoming the pulse shorting issue is still a major challenge for the researcher. The researchers have been continuously working to enhance the radio frequency (RF) output power of MILO by modifying its cathode structure, various types of anode structure, i.e., RF interaction structure, its output section, and using some techniques.

The preliminary theory of MILO and its experimental results were first reported by Clarke et al. [Clarke *et al*., *1988*]. Lemke et al. reported experimental studies on MILO using two different types of SWS, i.e., sinusoidal corrugated co-axial SWS and periodic disk-loaded co-axial SWS [Lemke *et al., 1997*]. The sinusoidal corrugated co-axial SWS-based MILO had a lower conversion efficiency, while periodic disk-loaded co-axial SWS-based MILO provides better conversion efficiency when compared with sinusoidal corrugated co-axial SWS-based MILO [Lemke *et al*., *1997*]. Furthermore, Haworth et al. identified some of the reasons for the pulse shortening problem related to the periodic disk-loaded structure and made some design improvements to remove this problem to some extent using the hard tube MILO [Haworth *et al*.,*1998*]. They further modified the position of the cathode structure alignment with choke and SWS and achieved RF output

power 2.5 times higher than the previously reported experiment [Haworth *et al*., *1998*]. Fan et al. experimentally reported an improved MILO in which they modified the beam dump region by introducing a disk and achieved 12% efficiency [Fan *et al*., *2007*]. Kumar et al. also improved the performance of MILO by optimizing the design parameter using impedance matching between different sub-sections of MILO [Kumar *et al*., *2019*]. Xu et al. reported a ridge MILO in which they improved the device conversion efficiency and obtained the frequency tunability by controlling the length of the ridge [Xu *et al*., *2020*]. The dielectric loading in the SWS cavity is another approach to improve the efficiency of the device. Another advantage of the dielectric loading also provides frequency tunability by changing the dielectric material and dielectric thickness. The concept of dielectric loading has already been used in various other microwave tubes such as gyrotron travelling wave tube (gyro-TWT), gyro-twystron, magnetron, and MILO [Rao *et al., 1996*- Singh *et al. 2018,*-Kesari *et al. 2005,*-Hashemi *et al., 2010*-Maurya *et al., 2012*-Fan *et al., 2015*]. The concept of dielectric loading in the device provides better options to enhance the device conversion efficiency and its frequency tuning. Therefore, the partially dielectric filled periodic disk-loaded co-axial SWS is analyzed here for MILO. To analyze the slow wave characteristics of any interaction structure, there are several approaches such as field matching approach, mode-matching approach, and equivalent circuit analysis approach [Kesari *et al. 2010*- Wang *et al., 2007*-Tripathi *et al., 2020*-Dwivedi *et al., 2012*- Dixit *et al., 2016*- Kumar *et al., 2020*- Kesari *et al., 2018]*.

In this chapter, the field matching approach is used to analyze the slow wave characteristics of the partially dielectric-filled axially periodic disk-loaded co-axial SWS for MILO. Using this performed analysis, one can easily explain the interaction impedance, phase velocity, and group velocity of the structure as well as this analysis also helps develop a better understanding of the structural parameter dependency on the above

mentioned parameter. In addition, using this analysis one can also obtain the dispersion characteristics for any symmetric TM modes which cannot obtained using the equivalent circuit analysis explained by Fan et al. In Section II, the relevant electromagnetic (EM) field expressions in different regions of the structure, boundary conditions, and the final expression of the dispersion relationship and interaction impedance for the symmetric TM mode are derived. In Section III, the results obtained from the analytical method and simulation tool are discussed in detail. Besides this, in this section, the parametric analysis is performed to understand the effect of different design parameters on the dispersion relationship and on the interaction impedance. The effect of the dielectric constant of the material on the dispersion characteristics and phase velocity is also investigated. Finally, the work has been summarized in Section IV.

2.3 Analytical approach

The periodic metal disk-loaded co-axial structure is widely used as an RF interaction structure in MILO. To improve the beam–wave interaction, the low-loss dielectric material with finite thickness is partially filled between consecutive metal disks. For analysis, only real part of dielectric constant (i.e., ε_r) is considered and it is assumed that the imaginary part of the dielectric constant is very small. Therefore, the value of loss tangent of the dielectric material is very small and the effect of the loss tangent can be ignored. The effect of the low-loss dielectric material is explained experimentally in [Zhang *et al. 2012*], in which very low-loss dielectric material was used whose loss tangent value was very low. The dielectric loading inside the interaction cavity increases the effective capacitance of the cavity which improves the energy storing capacity of the cavity. This stored RF energy is in the form of standing wave which is further coupled out by the extractor cavity which converts this standing wave into travelling wave. The schematic of the partially dielectric-filled periodic disk-loaded co-axial structure is shown

in Fig. 2.1. Fig. 2.1(a) shows the section view of the partially dielectric-filled periodic disk-loaded co-axial structure, and Fig. 2.1(b) shows its unit cell. For the analysis, the cylindrical coordinate system (r, θ, z) has been considered.

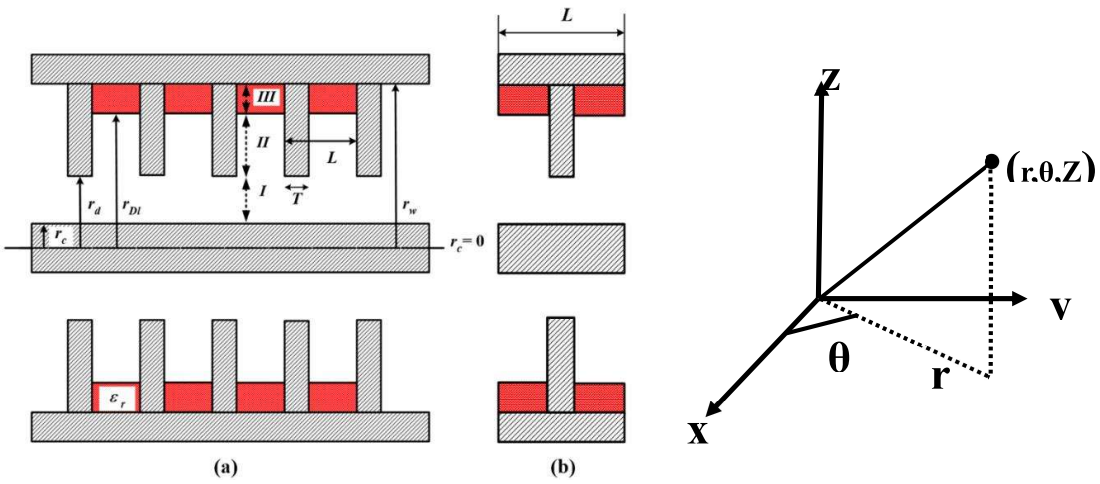

Fig 2.1: Schematic of dielectric-filled periodic disc loaded Co-axial structure **(a)** and **(b)** it's unit cell.

The interaction structure is separated into three regions; region-I [i.e., disk-free region ($r_c < r < r_d$)], region-II [i.e., disk occupied region ($r_d < r < r_{DI}$)], and region-III [i.e., partially dielectric-filled region ($r_{DI} < r < r_w$)]. In the structure (see Fig. 2.1), T is the thickness of the disk, L is the axial periodicity, r_d is the disk hole radius, r_w is the inner wall radius of the outer conductor, and r_c is the radius of the central co-axial conductor of the disk-loaded co-axial structure. The structure shows the axial periodicity with the period L, so the single unit cell of the structure [shown in Fig. 2.1(b)] is sufficient for analysis according to Fouquet's theorem. The field matching approach is chosen here to analyze this structure for TM modes ($H_z = 0$). Before analyzing the structure, some assumption has made such as the EM fields are time-independent, and there is a travelling wave in region-I while the standing waves are present in region-II and region-III. The axial periodicity of the structure is responsible for the space harmonics of travelling

waves, while the reflections from the metallic surfaces of the structure are responsible for the modal harmonics of standing waves. The parameters associated with different regions, i.e., regions-I–III, are superscripted with I–III, respectively.

2.3.1 EM Field Expression for Region-I (i.e., $r_c < r < r_d$)

For TM mode, the relevant field expressions for the disk free region under the slow wave regime can be written as [Tripathi *et al., 2020*- Dwivedi *et al., 2012*- Kumar *et al. 2020*].

$$H_Z^I = 0 \tag{2.1}$$

$$E_z^I = \sum_{n=-\infty}^{\infty} A_n^I \left\{ J_0\left(\gamma_n^I r\right) Y_0\left(\gamma_n^I r_c\right) - Y_0\left(\gamma_n^I r\right) J_0\left(\gamma_n^I r_c\right) \right\} \times e^{j\omega t - j\beta_n^I z} \tag{2.2}$$

The present analysis is carried out using ordinary Bessel function because the propagation constant which is obtained by solving the wave equation in the cylindrical system with the transverse propagation constant is considered as $\gamma_n^2 = k^2 - \beta_n^2$. For SWS, the argument of the Bessel function becomes real, and therefore an ordinary Bessel function is used to express the electric and magnetic field components (as explained in [Wang *et al.*], [Dwivedi *et al.*], and [Dixit *et al.*]). For the propagation constant, $\gamma_n^2 = \beta_n^2 - k^2$, the argument of Bessel function becomes imaginary, and therefore in place of ordinary Bessel function, modified Bessel function is used to express electric and magnetic field components (as explained in [Ghosh *et al. 1997*] and [B. N. Basu 1995]).

Using the above axial electric and magnetic field components, the remaining four electric and magnetic field components can be written with the help of Maxwell's equation as

$$
\begin{aligned}
E_r^{\Re} &= \left(\frac{-j}{\gamma_n^2}\right)\left\{\beta_n \frac{\partial E_z^{\Re}}{\partial r} + \frac{\omega\mu}{r}\frac{\partial H_z^{\Re}}{\partial \theta}\right\} \\
E_\theta^{\Re} &= \left(\frac{-j}{\gamma_n^2}\right)\left\{\frac{\beta_n}{r}\frac{\partial E_z^{\Re}}{\partial \theta} - \omega\mu\frac{\partial H_z^{\Re}}{\partial r}\right\} \\
H_r^{\Re} &= \left(\frac{j}{\gamma_n^2}\right)\left\{\frac{\omega\varepsilon}{r}\frac{\partial E_z^{\Re}}{\partial \theta} - \beta_n\frac{\partial H_z^{\Re}}{\partial r}\right\} \\
H_\theta^{\Re} &= \left(\frac{-j}{\gamma_n^2}\right)\left\{\omega\varepsilon\frac{\partial E_z^{\Re}}{\partial r} - \frac{\beta_n}{r}\frac{\partial H_z^{\Re}}{\partial \theta}\right\}
\end{aligned}
\tag{2.3}
$$

Here, superscript $\Re$ stands for components related to different regions (i.e., regions-I–III). The structure used for the analysis here is azimuthally symmetric, and therefore $(\partial/\partial\theta) = 0$. Substituting the above expression of the axial electric and magnetic field components given in (2.1) and (2.2), respectively, in (2.3), we can derive the remaining four field components as

$$
E_r^I = \sum_{n=-\infty}^{\infty} \frac{-j\beta_n^I}{\gamma_n^I} A_n^I \left\{J_0'\left(\gamma_n^I r\right) Y_0\left(\gamma_n^I r_c\right) - J_o\left(\gamma_n^I r\right) Y_0'\left(\gamma_n^I r_c\right)\right\} e^{j\omega t - j\beta_n^I z} \tag{2.4}
$$

$$
E_\theta^I = 0 \tag{2.5}
$$

$$
H_r^I = 0 \tag{2.6}
$$

$$
H_\theta^I = \sum_{n=-\infty}^{\infty} \frac{-j\omega\varepsilon_o}{\gamma_n^I} A_n^I \left\{J_0'\left(\gamma_n^I r\right) Y_0\left(\gamma_n^I r_c\right) - J_o\left(\gamma_n^I r\right) Y_0'\left(\gamma_n^I r_c\right)\right\} e^{j\omega t - j\beta_n^I z} \tag{2.7}
$$

In the above EM field expressions, $k\left(=\omega/c\right), k' = \omega\sqrt{\varepsilon_0\mu_o\varepsilon_r}$, $\gamma_n^I = \left(k^2 - \left(\beta_n^I\right)^2\right)^{1/2}$ and $\beta_n^I\left(=\beta_0 + 2n\pi/L\right)$ are the free-space propagation constant, the propagation constant in the presence of dielectric material, the radial propagation constant, and the axial propagation constant, respectively. Here, n (= 0, ±1, ±2, ±3,...) represents the number of space harmonics present in region-I, J_o and Y_o are the Bessel's function of the first and second

kind, respectively. The prime used as superscript (J_o' and Y_o') in the Bessel function indicates the first derivative of the Bessel function.

2.3.2 EM Field Expression for Region-II (i.e., $r_d < r < r_{DI}$)

The two consecutive disks that are separated by axial distance (L − T) show free space in region-II (i.e., disk present free-space region contains standing wave due to the reflections from the metal disk) producing an integral number of half guide wavelengths and can be written as [Tripathi *et al., 2020*- Dwivedi *et al., 2012*- Kumar *et al. 2020*].

$$\left(L-T\right)=\frac{m\lambda_m^{II}}{2} \qquad \left(m=1,2,3,.....\right) \tag{2.8}$$

Here, λ_m^{II} is the guided wavelength of stationary wave supported by region-II, and m (= 1, 2, 3 ...) is the stationary wave modal number. The relationship between half guide wavelengths (λ_m^{II}) and axial phase propagation constant (β_m^{II}) can be given as

$$\lambda_m^{II}=\frac{m\pi}{\beta_m^{II}} \tag{2.9}$$

Then, the relationship β_m^{II} for can be written with the help of (2.8) and (2.9), as

$$\beta_m^{II}=\frac{m\pi}{\left(L-T\right)} \qquad \left(m=1,2,3,.....\right) \tag{2.10}$$

The EM field expressions in region-II can be expressed as

$$E_z^{II}=\sum_{m=1}^{\infty}\left\{A_m^{II}J_o\left(\gamma_m^{II}r\right)+B_m^{II}Y_o\left(\gamma_m^{II}r\right)\right\}\times e^{j\omega t}Sin\left(\beta_m^{II}z\right) \tag{2.11}$$

$$E_r^{II} = \sum_{m=1}^{\infty} \frac{-j\beta_m^{II}}{\gamma_m^{II}} \left\{ A_m^{II} J_o'\left(\gamma_m^{II} r\right) + B_m^{II} Y_o'\left(\gamma_m^{II} r\right) \right\} \times e^{j\omega t} Sin\left(\beta_m^{II} z\right) \tag{2.12}$$

$$H_\theta^{II} = \sum_{m=1}^{\infty} \frac{-j\omega\varepsilon_o}{\gamma_m^{II}} \left\{ A_m^{II} J_o'\left(\gamma_m^{II} r\right) + B_m^{II} Y_o'\left(\gamma_m^{II} r\right) \right\} \times e^{j\omega t} Sin\left(\beta_m^{II} z\right) \tag{2.13}$$

Where β_m^{II}, $\gamma_m^{II}\left(=\sqrt{\left((k)^2 - \beta_m^2\right)}\right)$, and k are the axial propagation constant, radial propagation constant, and free-space propagation constant, respectively. A_m^{II} and B_m^{II} are the unknown coefficients. The remaining three EM field components (i.e., $E_\theta^{III}, H_z^{III}$, and H_r^{III}) become zero similar to region-I components [i.e., as explained above in (2.1), (2.5), and (2.6)].

2.3.3 EM Field Expression for Region-III (i.e., $r_{DI} < r < r_W$)

With reference to the m[th] stationary wave modal harmonic, the electric and magnetic field expressions in the dielectric filled region (i.e., region-III) with dielectric constant (ε_r) can be written as [Tripathi *et al., 2020*- Dwivedi *et al., 2012*- Kumar *et al. 2020*].

$$E_z^{III} = \sum_{m=1}^{\infty} \left\{ A_m^{III} J_0\left(\gamma_m^{III} r\right) + B_m^{III} Y_0\left(\gamma_m^{III} r\right) \right\} \times e^{j\omega t} Sin\left(\beta_m^{III} z\right) \tag{2.14}$$

Where

$$B_m^{III} = -\left(\frac{J_o\left(\gamma_m^{III} r_w\right)}{Y_o\left(\gamma_m^{III} r_w\right)} \right) A_m^{III}$$

Now rewriting the above equation by putting the value of B_m^{II}, we get

$$E_z^{III} = \sum_{m=1}^{\infty} \left\{ A_m^{III} \left\{ J_o\left(\gamma_m^{III} r\right) Y_o\left(\gamma_m^{III} r_w\right) - J_o\left(\gamma_m^{III} r_w\right) Y_o\left(\gamma_m^{III} r\right) \right\} \right\} \times e^{j\omega t} Sin\left(\beta_m^{III} z\right) \tag{2.15}$$

Where $\gamma_m^{III} = \sqrt{\left(\varepsilon_r K^2 - \beta_m^2\right)}$ is the radial propagation constant of region-III. Let it be reducing the expression by introducing a new constant $X_0\left(\gamma_m^{III} r\right)$

$$X_0\left(\gamma_m^{III} r\right) = \left\{ J_o\left(\gamma_m^{III} r\right) Y_o\left(\gamma_m^{III} r_w\right) - J_o\left(\gamma_m^{III} r_w\right) Y_o\left(\gamma_m^{III} r\right) \right\}$$

Thus

$$E_z^{III} = \sum_{m=1}^{\infty} \left\{ A_m^{III} X_0\left(\gamma_m^{III} r\right) \right\} e^{j\omega t} Sin\left(\beta_m^{III} z\right) \tag{2.16}$$

$$E_r^{III} = \sum_{m=1}^{\infty} \frac{-j\beta_m^{III}}{\gamma_m^{III}} A_m^{III} X_0'\left(\gamma_m^{III} r\right) \times e^{j\omega t} Sin\left(\beta_m^{III} z\right) \tag{2.17}$$

Where

$$X_0'\left(\gamma_m^{III} r\right) = \left\{ J_o'\left(\gamma_m^{III} r\right) Y_o\left(\gamma_m^{III} r_w\right) - J_o\left(\gamma_m^{III} r_w\right) Y_o'\left(\gamma_m^{III} r\right) \right\}$$

$$H_\theta^{III} = \sum_{m=1}^{\infty} \frac{-j\omega\varepsilon_o\varepsilon_r}{\gamma_m^{III}} X_0'\left(\gamma_m^{III} r\right) \times e^{j\omega t} Sin\left(\beta_m^{III} z\right) \tag{2.18}$$

Where $X_0'\left(\gamma_m^{III} r\right)$ is the first derivative of the expression $X_0'\left(\gamma_m^{III} r\right)$. The remaining three EM field expressions (i.e., E_θ^{III}, H_z^{III}, and H_r^{III}) become zero similar to region-I.

2.4 Boundary Conditions

The corresponding periodic metal disk-loaded co-axial structure here has two discontinuities, i.e., between region-I and region-II (for r = r_d) and the other between region-II and region-III (for r = r_{DI}). Therefore, the EM boundary conditions for this

structure can be written as follows.

The axial electric field intensity at the metallic surface (i.e., r = r_c, $0 \le \theta \le 2\pi$) can be stated as [Tripathi *et al., 2020*- Dwivedi *et al., 2012*- Kumar *et al. 2020*].

$$E_\theta^I = 0 \qquad 0 < z < \infty \tag{2.19}$$

1) For the boundary between region-I and region-II (at $r = r_d$)

$$E_z^I = \begin{cases} E_z^{II} & 0 < z < (L-T) \\ 0 & (L-T) < z < L \end{cases} \tag{2.20}$$

$$H_\theta^I = H_\theta^{II} \quad 0 < z < (L-T) \tag{2.21}$$

2) For the boundary between region-II and region-III (at $r = r_{Dl}$)

$$E_z^{II} = E_z^{III} \quad 0 < z < (L-T) \tag{2.22}$$

$$H_\theta^{II} = H_\theta^{III} \quad 0 < z < (L-T) \tag{2.23}$$

2.5 Dispersion Relationship

The field matching technique has been used to find out the dispersion relationship of the partially filled periodic metal disk-loaded co-axial structure. Using the above boundary conditions, a set of simultaneous equations have been obtained. These sets of simultaneous equations are arranged in the determinantal form which relates the wave frequency with the axial phase constant (or phase velocity).

2.5.1 For Regions-II and III:

To obtain the dispersion relationship for the partially dielectric-filled periodic disk-loaded co-axial waveguide structure, first, the electric field expression of region-II given in (2.11) and the electric field expression of region-III given in (2.14) are substituted into the boundary condition (2.20).

$$\sum_{m=1}^{\infty}\left\{A_m^{II}J_o\left(\gamma_m^{II}r_{Dl}\right)+B_m^{II}Y_o\left(\gamma_m^{II}r_{Dl}\right)\right\}\times Sin\left(\beta_m^{II}z\right)=\sum_{m=1}^{\infty}A_m^{III}X_0\left\{\gamma_m^{III}r_{Dl}\right\}Sin\left(\beta_m^{III}z\right)$$

Here, for the sake of simplicity, the time dependency has been ignored from derivation. The relationship between field coefficients can be obtained from the above expression as

$$A_m^{III}=\frac{J_0\left(\gamma_m^{II}r_{Dl}\right)}{X_0\left(\gamma_m^{III}r_{Dl}\right)}A_m^{II}+\frac{Y_0\left(\gamma_m^{II}r_{Dl}\right)}{X_0\left(\gamma_m^{III}r_{Dl}\right)}\beta_m^{II}$$

Similarly, $H_\theta^{II}=H_\theta^{III}$ at $r=r_{Dl}$

$$\sum_{m=1}^{\infty}\frac{-j\omega\varepsilon_o}{\gamma_m^{II}}\left\{A_m^{II}J_o'\left(\gamma_m^{II}r_{Dl}\right)+B_m^{II}Y_o'\left(\gamma_m^{II}r_{Dl}\right)\right\}\times Sin\left(\beta_m^{II}z\right)=\sum_{m=1}^{\infty}\frac{-j\omega\varepsilon_o\varepsilon_r}{\gamma_m^{III}}A_m^{III}X_0'\left\{\gamma_m^{III}r_{Dl}\right\}Sin\left(\beta_m^{III}z\right)$$

$$A_m^{III}=\frac{J_0\left(\gamma_m^{II}r_{Dl}\right)}{X_0\left(\gamma_m^{III}r_{Dl}\right)}A_m^{II}+\frac{Y_0\left(\gamma_m^{II}r_{Dl}\right)}{X_0\left(\gamma_m^{III}r_{Dl}\right)}\beta_m^{II}$$

So

$$\frac{J_0\left(\gamma_m^{II}r_{Dl}\right)}{X_0\left(\gamma_m^{III}r_{Dl}\right)}A_m^{II}-\frac{\gamma_m^{III}}{\varepsilon_r\gamma_m^{II}}\frac{J_0'\left(\gamma_m^{II}r_{Dl}\right)}{X_0'\left(\gamma_m^{III}r_{Dl}\right)}A_m^{II}=\left\{\frac{\gamma_m^{III}}{\varepsilon_r\gamma_m^{II}}\frac{Y_0'\left(\gamma_m^{II}r_{Dl}\right)}{X_0'\left(\gamma_m^{III}r_{Dl}\right)}-\frac{Y_0\left(\gamma_m^{II}r_{Dl}\right)}{X_0\left(\gamma_m^{III}r_{Dl}\right)}\right\}B_m^{II}$$

To reduce the equations, here new constant ξ, as shown below.

$$\frac{A_m^{II}}{B_m^{II}} = \frac{\varepsilon_r \gamma_m^{II} X_0'\left(\gamma_m^{III} r_{Dl}\right) J_0\left(\gamma_m^{II} r_{Dl}\right) - \gamma_m^{III} X_0\left(\gamma_m^{III} r_{Dl}\right) J_0'\left(\gamma_m^{II} r_{Dl}\right)}{-\varepsilon_r \gamma_m^{II} X_0'\left(\gamma_m^{III} r_{Dl}\right) Y_0\left(\gamma_m^{II} r_{Dl}\right) + \gamma_m^{III} X_0\left(\gamma_m^{III} r_{Dl}\right) Y_0'\left(\gamma_m^{II} r_{Dl}\right)} = \xi$$

Now applying boundary condition (2.23), we obtained

$$\sum_{m=1}^{\infty}\left\{A_m^{II} J_o\left(\gamma_m^{II} r_d\right) + B_m^{II} Y_o\left(\gamma_m^{II} r_d\right)\right\} \times Sin\left(\beta_m z\right) = \sum_{n=-\infty}^{\infty} A_n^{I}\left\{J_o\left(\gamma_n^{I} r_d\right) Y_0\left(\gamma_n^{I} r_c\right) - J_o\left(\gamma_n^{I} r_c\right) Y_0\left(\gamma_n^{I} r_d\right)\right\} e^{-j\beta_n Z}$$

Now, multiplying both sides by $Sin\left(\beta_m Z\right)$ and integrating from 0 to (L-T), we get

$$\sum_{m=1}^{\infty}\left\{A_m^{II} J_o\left(\gamma_m^{II} r_d\right) + \xi A_m^{II} Y_o\left(\gamma_m^{II} r_d\right)\right\} \int_0^{L-T} Sin^2\left(\beta_m z\right) dz =$$

$$\sum_{n=-\infty}^{\infty} A_n^{I}\left\{J_o\left(\gamma_n^{I} r_d\right) Y_0\left(\gamma_n^{I} r_c\right) - J_o\left(\gamma_n^{I} r_c\right) Y_0\left(\gamma_n^{I} r_d\right)\right\} \int_0^{L-T} Sin\left(\beta_m z\right) \times e^{-j\beta_n Z} dz$$

After integrating the above expression, we obtained,

$$A_m^{II}\left\{J_o\left(\gamma_m^{II} r_d\right) + \xi Y_0\left(\gamma_m^{II} r_d\right)\right\} \times \left[\frac{L-T}{2}\right] =$$

$$\sum_{n=-\infty}^{\infty} A_n^{I}\left\{J_o\left(\gamma_n^{I} r_d\right) Y_0\left(\gamma_n^{I} r_c\right) - J_o\left(\gamma_n^{I} r_c\right) Y_0\left(\gamma_n^{I} r_d\right)\right\} \times \frac{\beta_m}{\beta_n^2 - \beta_m^2}\left[\left(-1\right) + \left(-1\right)^m \exp\left(-j\beta_n\left(L-T\right)\right)\right]$$

Thus, the expression can be rewritten as,

$$A_m^{II} = \sum_{n=-\infty}^{\infty} A_n^{I} S_{n,m} \qquad \left(\text{at } r = r_d \text{ and } L-T < z < L\right) \tag{2.24}$$

Let introducing a new constant $S_{n,m}$ to reduce the expression

$$S_{n,m} = \sum_{n=-\infty}^{\infty}\left\{\frac{J_0\left(r_n^{I} r_d\right) Y_0\left(r_n^{I} r_c\right) - J_0\left(r_n^{I} r_c\right) Y_0\left(r_n^{I} r_d\right)}{J_0\left(r_m^{II} r_d\right) + \xi Y_0\left(r_m^{II} r_d\right)}\right\} \times$$

$$\times\left\{\frac{2\beta_m}{\left(L-T\right)\left(\beta_n^2 - \beta_m^2\right)}\left(\left(-1\right) + \left(-1\right)^m \exp\left(-j\beta_n L\right)\right)\right\}$$

2.5.2 For Regions-II and I:

Similarly, the relationship can be established between unknowns present in the region-II and region-I. The electric field expression of region-I given in (2.2) and the electric field expression of region-II given in (2.11) are applied into the boundary condition (2.20). The expressions obtained after applying the boundary condition are multiplied by ($Sin(\beta_m z)$) and then integrating that resultant expression between limits 0 < z < (L − T), we get the relationship between A_m^I and A_n^I. Now applying the boundary condition (2.21), we get

$$\sum_{m=1}^{\infty} \frac{-j\omega\varepsilon_o}{\gamma_m^{II}} \left\{ A_m^{II} J_o'\left(\gamma_m^{II} r_d\right) + \xi A_m^{II} Y_o'\left(\gamma_m^{II} r_d\right) \right\} \times Sin(\beta_m z) =$$

$$\sum_{n=-\infty}^{\infty} \frac{-j\omega\varepsilon_o}{\gamma_n^I} A_n^I \left(J_0'\left(\gamma_n^I r_d\right) Y_0\left(\gamma_n^I r_c\right) - J_0\left(\gamma_n^I r_c\right) Y_0'\left(\gamma_n r_d\right) \right) e^{-j\beta_n z}$$

Multiplying both sides by $Sin(\beta_m z)$ and integrating from 0 to (L − T), we get the relationship between A_m^{II} and A_n^{II}, that is,

$$A_m^{II} = \sum_{n=-\infty}^{\infty} \left\{ \left\{ \frac{2\beta_m \gamma_m^{II}}{\left(\beta_n^2 - \beta_m^2\right)(L-T)\gamma_n^I} \right\} \left[(-1) + (-1)^m \exp\left(-j\beta_n (L-T)\right) \right] \times \right.$$

$$\left. \times \left\{ \frac{J_o'\left(\gamma_n^I r_d\right) Y_0\left(\gamma_n^I r_c\right) - J_o\left(\gamma_n^I r_c\right) Y_0'\left(\gamma_n^I r_d\right)}{J_o'\left(\gamma_m^{II} r_d\right) + \xi Y_0'\left(\gamma_m^{II} r_d\right)} \right\} \right\} A_n^I$$

and thus we obtain

$$A_m^{II} = \sum_{n=-\infty}^{\infty} U_{n,m} A_n^I \tag{2.25}$$

For reducing the expression introducing a new constant $U_{n,m}$. So

$$U_{n,m}=\sum_{n=-\infty}^{\infty}\left\{\frac{2\beta_m\gamma_m^{II}}{\left(\beta_n^2-\beta_m^2\right)\left(L-T\right)\gamma_n^I}\right\}\left[\left(-1\right)+\left(-1\right)^m\exp\left(-j\beta_n\left(L-T\right)\right)\right]\times$$
$$\times\left\{\frac{J_o'\left(\gamma_n^I r_d\right)Y_0\left(\gamma_n^I r_c\right)-J_o\left(\gamma_n^I r_c\right)Y_0'\left(\gamma_n^I r_d\right)}{J_o'\left(\gamma_m^{II} r_d\right)+\xi Y_0'\left(\gamma_m^{II} r_d\right)}\right\}$$

Now, as given in (2.24) and (2.25) both represented A_m^{II} in the form of region-I constant A_n^I, and thus after equating both the expressions and doing some needful derivation, we obtained the following expression:

$$\sum_{n=-\infty}^{\infty}\left(S_{n,m}-U_{n,m}\right)A_n^I=0 \tag{2.26}$$

Expression (2.24) is formed m number of simultaneous series equations of the EM field constant A_n^I where A_n^I itself is of an infinite number ($-\infty < n < \infty$). Solving these simultaneous equations for a nontrivial solution, one may use the determinant method. To find the dispersion relationship of the structure, the determinant of the order m ×n is formed which is set to zero. The final dispersion relationship can be obtained as

$$\det|S_{n,m}-U_{n,m}| = 0\ (-\infty < n < \infty,\ 1 \le m < \infty) \tag{2.27}$$

Expression (2.27) is a set of an infinite number of space harmonics and also stationary wave modes. Here, “det” is the abbreviation of determinant. The determinant which is given above has an infinite number of co-efficient which should be truncated up to some extent (i.e., some finite order) for solving the above dispersion relationship given in (2.27).

2.6 Interaction Impedance (K)

The interaction impedance (K) is considered an essential parameter that helps in estimating the efficient interaction between RF wave and electron beam. In the MILO device, as TM mode is supported by the structure, the axial electric field component E_z is mainly responsible for energy transfer between electron beam and RF wave, whereas the

radial electric field E_r is responsible for electron beam bunching formation. As per the definition, the interaction impedance is given as [Tripathi *et al. 2020*], [Dwivedi *et al. 2012*], [Kesari *et al*., *2018* - Zhang *et al*., *2012* - Ghosh *et al*., *1997* - B.N. Basu *1995*].

$$K = \frac{\left|E_{zn}\right|^2}{2\beta_n^2 P} \tag{2.28}$$

Here, $|E_{zn}|$ is the magnitude of the axial electric field, β_n is the axial phase propagation constant and P is the total transmitted RF power through the structure. For the MILO device, the electron beam and RF wave interaction mainly occurs in the region-I. The total transmitted RF power through the structure can be written as

$$P = \frac{1}{2}\int_{r_c}^{r_d}\int_{0}^{2\pi}\left(E_r^I H_\theta^{I^*} - E_\theta^I H_r^{I^*}\right) r dr d\theta \tag{2.29}$$

As the above equation is derived for symmetric *TM* mode so, H_θ^I and $H_r^I = 0$. Now the expression (2.29) can be rewritten as,

$$P = \frac{1}{2}\int_{r_c}^{r_d}\int_{0}^{2\pi}\left(E_r^I H_\theta^{I^*}\right) r dr d\theta \tag{2.30}$$

As the above equation is derived for symmetric TM mode, E_r^I and H_θ^I. Now the above expression can be

$$P = \sum_{n=-\infty}^{\infty} \frac{\pi\beta_n^I \omega\varepsilon}{\left(\gamma_n^I\right)^2}\left\{E_n^I\left(\gamma_n^I r\right)\right\}^2\left(A_n^I\right)^2 .rdr \tag{2.31}$$

The magnitude of the axial electric field can be obtained using (2.2) as

$$\left|E_{zn}\right|^2 = \sum_{n=-\infty}^{\infty}\left\{A_n^I J_0\left(\gamma_n^I r\right) + B_n^I Y_0\left(\gamma_n^I r\right)\right\}^2 \tag{2.32}$$

The relation between EM field constant A_n^I and B_n^I present in the above expression (2.32) can be given as,

$$B_n^I = -\frac{J_0\left(\gamma_n^I r_c\right)}{Y_0\left(\gamma_n^I r_c\right)} A_n^I \tag{2.33}$$

Finally, by substituting the above equation (2.31) and (2.32) in equation (2.28), the final interaction impedance can be obtained and given as,

$$K_{z,n} = \frac{\left\{E_0^I\left(\gamma_0^I r\right)\right\}^2}{\frac{\pi\beta_0^I \omega\varepsilon}{\left(\gamma_0^I\right)^2}\int_{r_c}^{r_d}\left\{E_0^I\left(\gamma_0^I r\right)\right\}^2 .rdr \times \left(2\beta_n^2\right)} \tag{2.34}$$

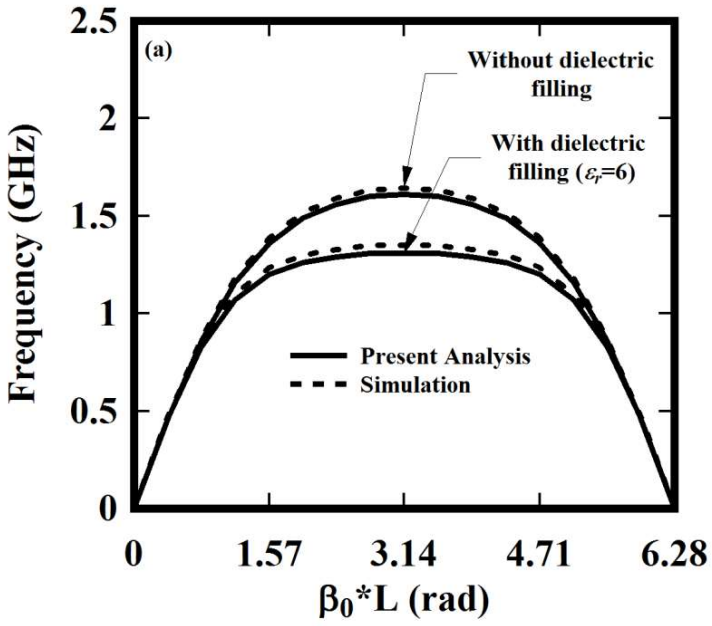

Fig. 2.2. Dispersion characteristics of the partially dielectric-filled axially periodic disk-loaded co-axial SWS with structural parameter with r_c = 29 mm, r_d = 43 mm, r_w = 87 mm, L = 20 mm, and T = 3 mm. **(a)** Comparison between numerically obtained and simulation obtained dispersion characteristics.

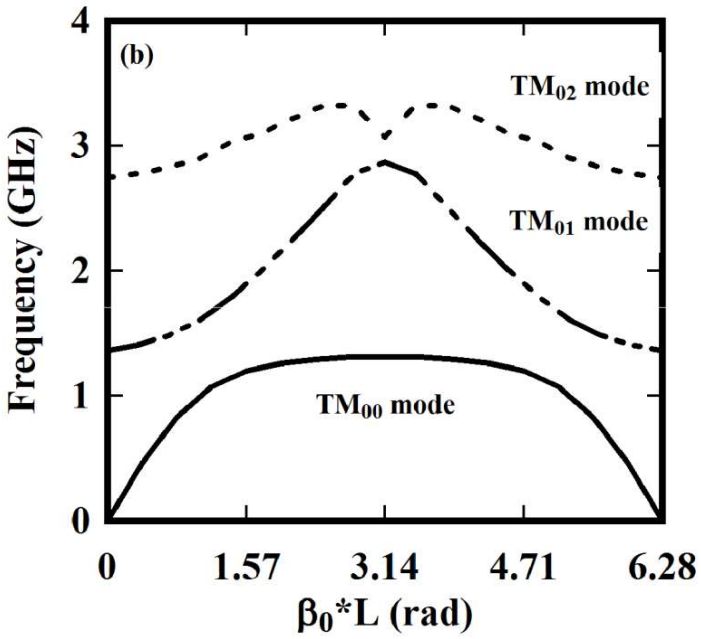

Fig. 2.2. Dispersion characteristics of the partially dielectric-filled axially periodic disk-loaded co-axial SWS with structural parameter with r_c = 29 mm, r_d = 43 mm, r_w = 87 mm, L = 20 mm, and T = 3 mm. **(b)** Different azimuthally symmetric TM modes.

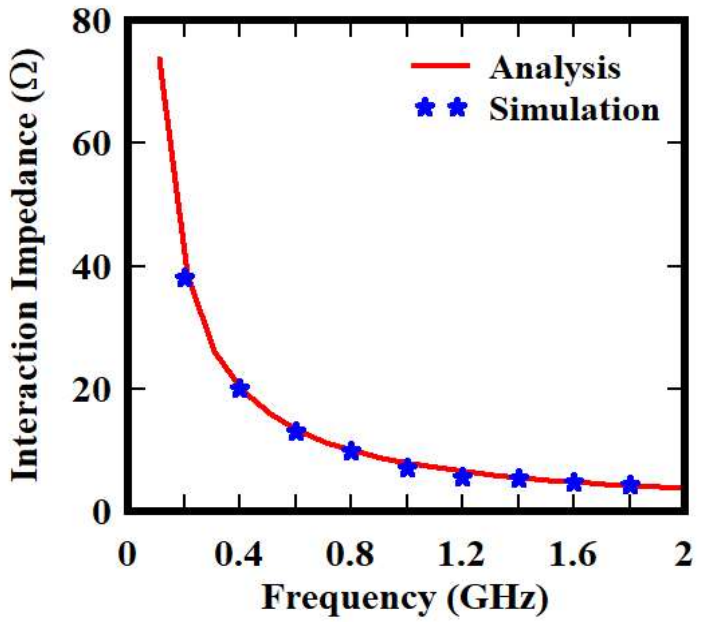

Fig. 2.3. Comparison between interaction impedance obtained through numerical analysis and simulation.

2.7 Results and discussion

With the objective of beam–wave interaction enhancement, the partially dielectric-filled axially periodic disk-loaded coaxial structure as an interaction structure for MILO is analyzed. The above analysis has been performed with the mind-set that this analysis highlights the effect of different structural parameters of SWS and helps in identifying the crucial structural parameters of the structure which affect the dispersion parameter at most. To find the operating frequency (i.e., π-mode frequency), and the effect of the dielectric loading on the desired operational mode of the structure, the dispersion relationship is considered as one of the vital tools. After getting the dispersion relationship, the analysis has been further extended to calculate the interaction impedance of the structure. The interaction impedance of the structure is a very crucial parameter that helps in understanding the mechanism the beam–wave interaction and also in optimizing the parameter of the structure. To verify the analysis, the structure has been designed according to the reported design data for the L-band MILO in [Fan *et al. 2015*]. Since according to Floquet's theorem the single unit of the periodic structure is sufficient for the analysis, the unit structure is used here for simulation. This technique is also helpful to reduce the memory requirement and simulation time. The single unit of the structure is designed and simulated by providing the appropriate boundary values in the eigenmode solver module of the "Computer Simulation Tool (CST) Studio Suite" [User Manual *2017*]. The dispersion characteristics obtained from the numerical analysis and from the EM simulation tool are shown in Fig. 2.2(a). From the figure, it is noted that the dispersion characteristics obtained through numerical analysis and EM tool in the presence and absence of the dielectric loading are in good agreement and the relative difference between them is below 5%. The main reason behind this difference is some approximation which was used to perform this numerical analysis. Another reason behind

this discrepancy is that simulation is always done under ideal conditions. The dispersion characteristics for different azimuthally symmetric TM modes obtained using the analysis are shown in Fig. 2.2(b). The interaction impedance of SWS is mainly used to understand the beam–wave interaction within SWS. Figure. 2.3 shows the interaction impedance obtained with the help of numerical analysis and EM tool.

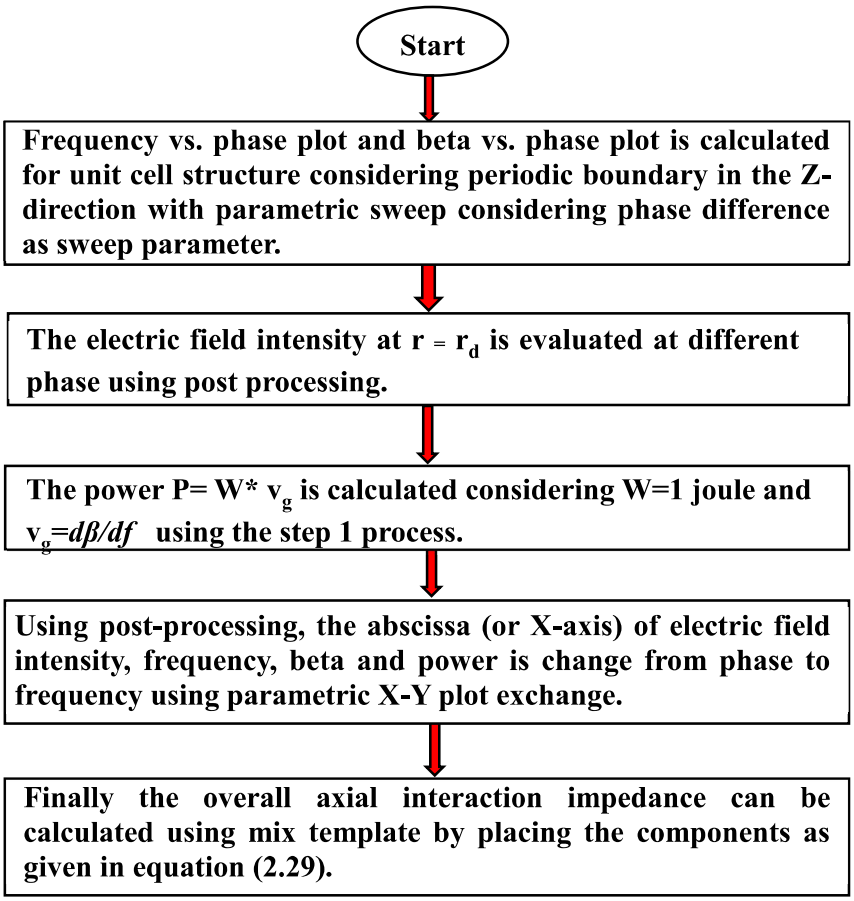

Fig. 2.4. Flowchart for calculating interaction impedance using EM simulation tool "CST."

From Fig. 2.3, it is noted that the numerically obtained interaction impedance follows the interaction impedance obtained from EM tool which also validates with the performed analysis. As MILO is a low-impedance device, the interaction impedance

should be compatible with the device's characteristic impedance. The interaction impedance of the structure is calculated numerically with the help of expression (2.34), while the simulated interaction impedance is obtained by the eigenmode solver module of the CST Studio Suite. The process involved in calculating the interaction impedance using CST simulation tool is explained with the help of a flowchart which is given in Fig. 2.4. Furthermore, the effect of different dielectric constants on the dispersion characteristics of the fundamental mode (i.e., TM_{00} mode) is obtained for the partially dielectric-filled axially periodic disk-loaded co-axial structure. Fig. 2.5 shows the effect of dielectric constant on the dispersion characteristics. The figure shows that as the dielectric constant of the material is increased, the overall dispersion characteristics decrease which means that the frequency associated with the π-mode of the structure decreases. The phase velocity of the EM field inside the structure with respect to the phase difference of consecutive cavity and with respect to different frequencies is shown in Fig. 2.6. The phase velocity is normalized by the speed of light. From the figure, it is noted that as the dielectric constant of the material increases, the associated phase velocity decreases. The dielectric constant increases the effective capacitance of the cavity which causes a decrease in the phase velocity as the phase velocity is inversely proportional to the effective capacitance of the cavity. Since the normalized phase velocity is less than 1 (observed from Fig. 2.6), it can be concluded that the structure is analyzed in a slow wave.

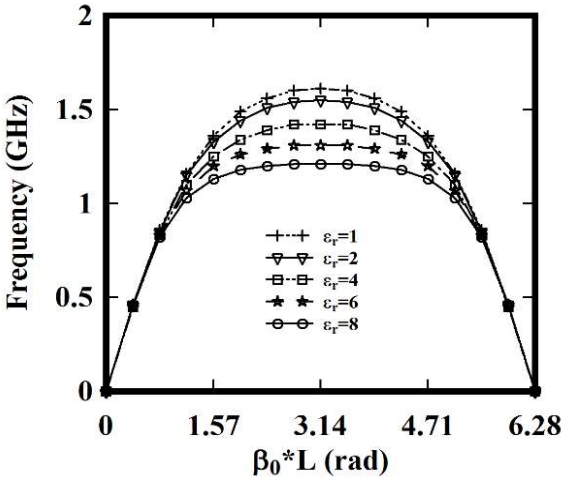

Fig. 2.5. Dispersion relation for the dielectric-filled axially periodic disc loaded coaxial waveguide structure with $0 < z < L - T$ mm, $r_c = 29$ mm, $r_d = 43$ mm, $r_w = 87$ mm, $L = 20$ mm, and $T = 3$ mm.

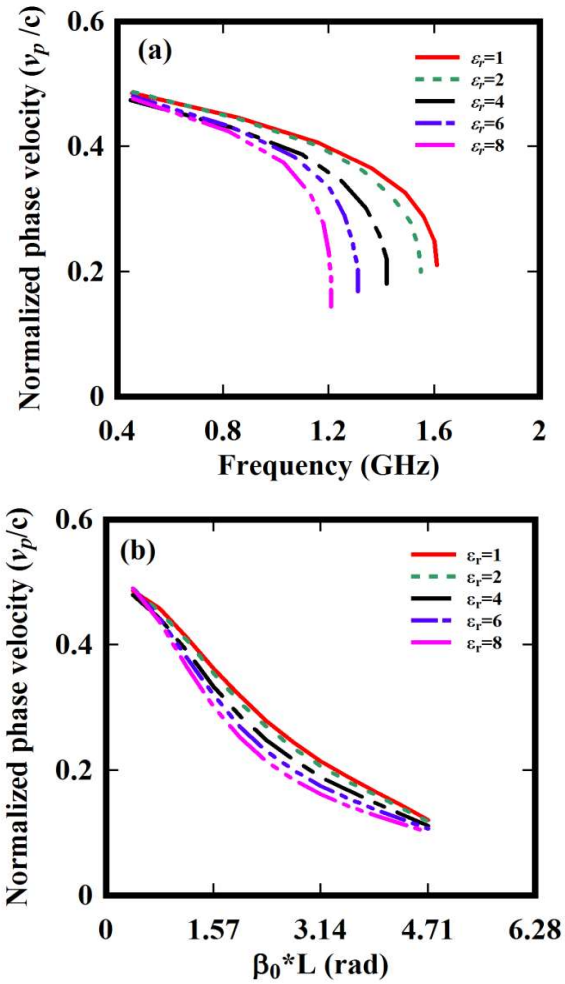

Fig. 2.6. (a) Normalized phase velocity versus frequency. **(b)** Normalized phase velocity versus phase difference between consecutive cavities.

2.7.1 Parametric Study on Dispersion Relationship

To overlook the dependency of structural parameters on the dispersion characteristics (i.e., operating frequency), the parametric study has been performed. The operating frequency of the MILO mainly depends on the structural parameters of SWS, and therefore the parametric analysis is performed to identify the critical design parameters of the structure. Fig. 2.7 shows the effect of various design parameters on the dispersion characteristics. Fig. 2.7(a)–(d) shows the effect of cathode radius (r_c), disk inner radius (r_d), inner wall radius (r_w), and periodicity of disk loading (L), respectively. From Fig. 2.7(a), it is observed that the variation in the cathode radius produces an insignificant change in the dispersion characteristics. Fig. 2.7(b) depicts the effect of the disk inner radius on the dispersion characteristics. From the figure, it is observed that with an increase in the radius of the disk, the curve of the dispersion characteristics shifted in an upward direction which shows the increase in π-mode frequency. The effect of the inner wall radius on the dispersion characteristics is shown in Fig. 2.7(c). From the figure, it is observed that as the radius of the inner wall increases, the curve of the dispersion characteristics shifted in the downward direction which indicates the decrement in π-mode frequency. In the end, the effect of disk periodicity on the dispersion characteristics is shown in Fig. 2.7(d). From the figure, it is observed that the effect of disk periodicity is negligible on the dispersion characteristics but the disk periodicity has a significant effect on the phase velocity which is a crucial parameter in the beam–wave interaction mechanism. Finally, from the parametric analysis, it is concluded that only the disk inner

radius and inner wall radius are the most significant parameters of the structure which affects the dispersion characteristics at most.

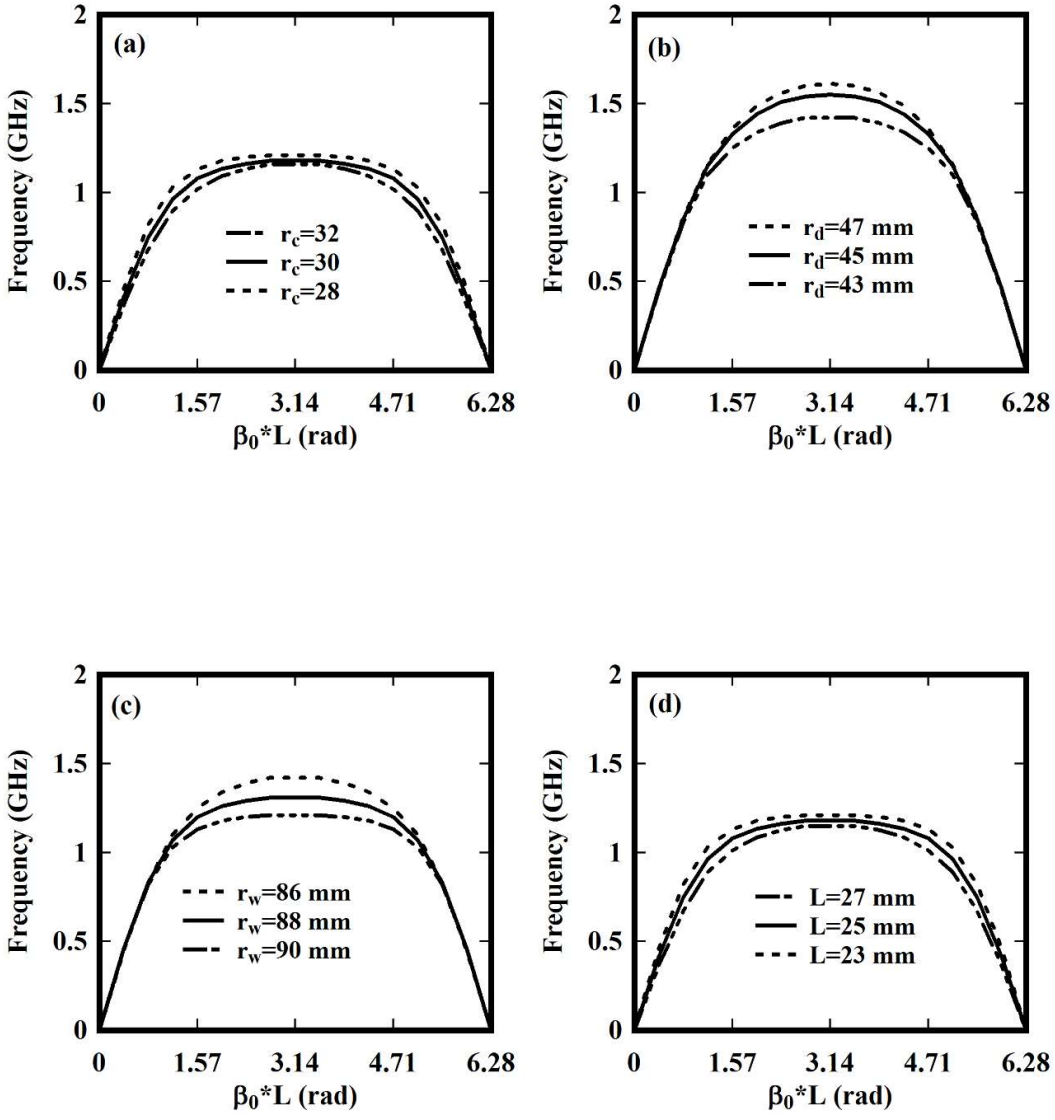

Fig. 2.7. Parametric effect on dispersion relationship **(a)** Effect of r_c . **(b)** Effect of r_d . **(c)** Effect of r_w . **(d)** Effect of L.

2.7.2 Parametric Study on Interaction Impedance

In this section, the effect of different structural parameters on interaction impedance has been studied. The effect of different structural parameters on interaction impedance is depicted in Fig. 2.8. Figures. 2.8(a) and (b) shows the effect of cathode radius (r_c), and disk inner radius (r_d), respectively. From Fig. 2.8(a), it is observed that as the cathode radius (r_c) increases, the interaction impedance increases, while from Fig. 2.8(b) it is observed that an increase in the disk inner radius (r_d) decreases the interaction impedance significantly. Thus, from the figures, it is concluded that the disk inner radius (r_d) is a significant structural parameter when compared with other structural parameters.

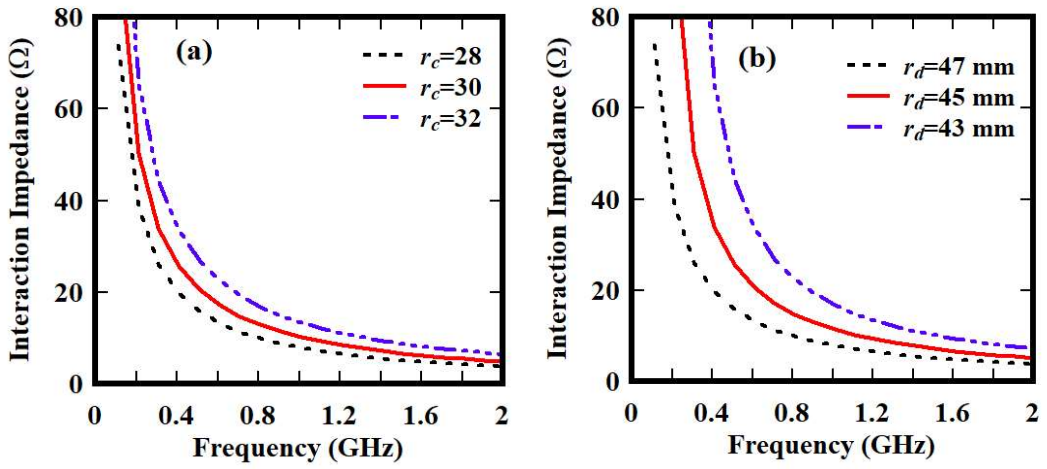

Fig. 2.8. Effect of structure design parameters on interaction impedance**. (a)** Effect of cathode radius r_c . **(b)** Effect of a disk inner radius r_d .

2.8 Conclusion

The partially dielectric-filled axially periodic disk-loaded co-axial SWS was analyzed as an interaction structure for MILO. The field matching technique was used to calculate its dispersion relationship and interaction impedance in the absence of an electron beam (i.e., cold analysis). The dispersion characteristics and interaction impedance are vital relationships for any beam–wave interaction structure to identify the operating frequency and also help in finding the design parameter of the device at which efficient beam–wave interaction takes place. The effect of the dielectric constant of the material on the dispersion characteristics and phase velocity was investigated. Also, the effect of different structural parameters of the structure on the dispersion characteristics and the interaction impedance were calculated. For validation, the dispersion characteristics obtained through numerical analysis were compared with the dispersion characteristics obtained from the CST Studio Suite. The agreement between theoretical analysis and simulation was below 5% which verifies the performed theoretical analysis. This study was performed with the aim that it enhances the understanding of structural dependency on the dispersion characteristics and might be helpful to design engineers who are working on HPM device MILO.